



Thermal Conductivities and Thermal Expansion Coefficients of $(\text{Sm}_{0.5}\text{Gd}_{0.5})_2(\text{Ce}_{1-x}\text{Zr}_x)_2\text{O}_7$ Ceramics

Zhang Hongsong, Shi Lei, Zhao Yongde, Li Gang, and Li Zhenjun

(Submitted February 8, 2015; in revised form May 9, 2015; published online July 23, 2015)

The $(\text{Sm}_{0.5}\text{Gd}_{0.5})_2(\text{Ce}_{1-x}\text{Zr}_x)_2\text{O}_7$ oxides were prepared by solid-state reaction, and their phase compositions, microstructures, and thermophysical properties were investigated. Results of x-ray diffraction reveal that pure $(\text{Sm}_{0.5}\text{Gd}_{0.5})_2(\text{Ce}_{1-x}\text{Zr}_x)_2\text{O}_7$ oxides with fluorite structure are successfully synthesized in the current study. The thermal expansion coefficient decreases with increasing content of ZrO_2 , which is higher than that of 7 wt.% yttria-stabilized zirconia (YSZ). The substitution of Zr^{4+} for Ce^{4+} reduces the thermal conductivity of $\text{Sm}_2\text{Ce}_2\text{O}_7$ oxide. The thermal conductivity decreases from 1.69 W/m K ($x = 0$) to 1.22 W/m K ($x = 0.3$) at 1000 °C. The composition with $x = 0.3$ exhibits the lowest thermal conductivity at all temperatures, and the thermal conductivity of $(\text{Sm}_{0.5}\text{Gd}_{0.5})_2(\text{Ce}_{1-x}\text{Zr}_x)_2\text{O}_7$ ceramics was obviously lower than those of fully dense 7 wt.% YSZ. These results suggested promising potential applications of the $(\text{Sm}_{0.5}\text{Gd}_{0.5})_2(\text{Ce}_{1-x}\text{Zr}_x)_2\text{O}_7$ ceramics for high-temperature thermal barrier coatings.

Keywords ceramics, coatings, rare earth, thermal barrier coatings, thermal conductivity

1. Introduction

Gas turbines operate at high temperatures where phenomena such as oxidation and creep occur readily. Thermal barrier coating (TBC) systems have become common in gas turbines as they lower the temperature of the underlying substrate and provide protection against high-temperature degradation of the substrate materials (Ref 1). TBC systems thus prolong the life of structural parts, as well as increase the gas turbine efficiency by enabling higher combustion temperatures (Ref 2–4). The requirements to improve jet engine efficiencies have proved to be a big driving force to improve the thermal barrier coating technology by novel compositions and improved production techniques for subsequent improvement in microstructure and thus enhance thermo-mechanical performance of TBCs. Yttria-stabilized zirconia (YSZ) is the present industrial standard topcoat material in TBC system, which can operate long term at temperatures below 1200 °C (Ref 5, 6). However, two flaws, including phase transformation and sintering, have been reported when YSZ is exposed to high temperature (above 1200 °C) for long time. Met stable tetragonal phase decomposes into tetragonal and cubic phase above 1200 °C. Upon cooling, tetragonal phase transforms to monoclinic phase, causing about 3.5% volume change and resulting in crack

formation in the TBCs. In addition, volume fraction of pores decreases due to the significant sintering of YSZ at high temperature, which leads to an increase in the thermal conductivity as well as the in-plane stiffness and thus decreases the strain compliance of TBCs (Ref 7–9). The limited capability of YSZ above 1200 °C necessitates its substitution with some novel compositions capable of handling higher temperatures with better stability in advanced gas turbines (Ref 10, 11).

A number of oxide ceramics have been proposed as novel thermal barrier coatings during the last few years. These novel compositions cover especially doped zirconia (Ref 12, 13), pyrochlores (Ref 14, 15), aluminates (Ref 16, 17), and perovskites (Ref 10). Recently, $\text{Sm}_2\text{Ce}_2\text{O}_7$ has been investigated as one TBC candidate material because of its better thermal properties (Ref 18). In order to enhance the performance of this $\text{A}_2\text{B}_2\text{O}_7$ compounds, co-doping on the A-site by one or more oxide has been proposed to reduce the thermal conductivity (Ref 19–22). Ying doped $\text{La}_2\text{Zr}_2\text{O}_7$ with Yb_2O_3 (Ref 14), and G. Z. Liu doped $\text{Gd}_2\text{Zr}_2\text{O}_7$ with Nd_2O_3 (Ref 15), and their thermal conductivities were further reduced after doping. Clarke and coworkers also pointed out that substituted atoms at site B create mass disorder on the cation sublattice, which results in the lowering of thermal conductivity (Ref 23). Ying investigated the thermophysical properties of Ce-doped $\text{La}_2\text{Zr}_2\text{O}_7$, and found that the doped ceramics $(\text{La}_{0.7}\text{Yb}_{0.3})_2(\text{Zr}_{0.7}\text{Ce}_{0.3})_2\text{O}_7$ and $(\text{La}_{0.2}\text{Yb}_{0.8})_2(\text{Zr}_{0.7}\text{Ce}_{0.3})_2$ have lower thermal conductivity than $\text{La}_2\text{Zr}_2\text{O}_7$, whereas their thermal expansion coefficient are higher than $\text{La}_2\text{Zr}_2\text{O}_7$ (Ref 14). Wan found that Ti substitution for Zr can reduce significantly thermal conductivity at lower temperatures, and the maximum value of thermal expansion coefficient is obtained at $x = 0.2$ (Ref 24). Ling indicated that $\text{Sm}_2\text{Zr}_2\text{O}_7$ co-doped with La_2O_3 , Yb_2O_3 , and CeO_2 has lower thermal conductivity and high thermal expansion coefficient as compared to $\text{Sm}_2\text{Zr}_2\text{O}_7$ (Ref 25). However, no research has been conducted concerning B-site substitution of SmCe_2O_7 . In this paper, the Gd^{3+} and Zr^{4+} were selected to partially substitute the Sm^{3+} and Ce^{4+} in order to provide a general insight into the involvement of thermophysical properties on B-site doping of $\text{A}_2\text{Ce}_2\text{O}_7$ -type fluorite.

Zhang Hongsong, Institute of Chemistry Henan Academy of Sciences, Zhengzhou 450002, China and School of Mechanical Engineering, Henan Institute of Engineering, Zhengzhou 451191, China; **Shi Lei**, Department of Locomotive and Rolling Stock, Zhengzhou Railway Vocation Technical College, Zhengzhou 45007, China; **Zhao Yongde**, Institute of Chemistry Henan Academy of Sciences, Zhengzhou 450002, China; and **Li Gang** and **Li Zhenjun**, School of Mechanical Engineering, Henan Institute of Engineering, Zhengzhou 451191, China. Contact e-mail: zhs761128@163.com.

2. Experimental

In this paper, the polycrystalline samples of the $(\text{Sm}_{0.5}\text{Gd}_{0.5})_2(\text{Ce}_{1-x}\text{Zr}_x)_2\text{O}_7$ ceramics were synthesized by a solid-state reaction method. Sm_2O_3 , Gd_2O_3 , ZrO_2 , and CeO_2 with purity 99.9% were used as starting materials, and all oxides were dried before use. The stoichiometric amounts of precursors were ground in acetone for 6 h to obtain uniformly distributed mixtures. The mixture slurry was dried at 120 °C for 2 h for complete removal of acetone. The dried powders were pressed into small columns at 50 MPa followed by cold isostatic pressing with 150 MPa. Finally, the bulks were pressureless sintered at 1600 °C for 10 h in air.

The phase structure of $(\text{Sm}_{0.5}\text{Gd}_{0.5})_2(\text{Ce}_{1-x}\text{Zr}_x)_2\text{O}_7$ oxides was identified by x-ray diffraction (XRD, Rigaku D/Max 2500, Japan) with Ni-filtered Cu K α radiation (0.1542 nm) at the scanning rate of 4°/min. The microstructure of the pellets was observed using field emission scanning electron microscopy (SEM, Model Hitachi S-4800, Japan). The specimens were polished with 1- μm diamond paste, and then thermally etched at 1500 °C for 2 h in air for SEM observations. Qualitative x-ray element analysis of various phases was carried out using SEM equipped with energy dispersive spectroscopy (EDS). For heat-treated samples, the actual densities (ρ) were measured by using Archimedes method with an immersion medium of deionized water.

The thermal expansion coefficients of these ceramics were determined with a high-temperature dilatometer (Netzsch DIL402C/7, Germany) from ambient temperature to 1000 °C at a heating rate of 5°/min in argon atmosphere. The size of sample was 25 mm \times 3 mm \times 4 mm. The specific heat capacities (C_p) were calculated from constituent oxides according to the Neumann-Kopp rule based on the reference specific heat values of Sm_2O_3 , Gd_2O_3 , CeO_2 , and ZrO_2 (Ref 26). The thermal diffusivity (λ) was measured from 200 to 1000°C using a laser flash apparatus (FlashLineTM3000, USA) in an argon gas atmosphere. The specimen dimension was about 12.7 mm in diameter and about 1.2 mm in thickness. The thermal conductivity was then calculated according to the relation:

$$k = \lambda \cdot \rho \cdot C_p. \quad (\text{Eq 1})$$

Because the sintered specimen was not fully dense, the measured thermal conductivity was modified for the actual value k_0 using Eq 2, where ϕ is the fractional porosity and the coefficient 4/3 is used to eliminate the effect of porosity on actual thermal conductivity (Ref 17).

$$k/k_0 = 1 - \frac{4}{3}\phi. \quad (\text{Eq 2})$$

3. Results and Discussions

3.1 Phase Structure

The XRD patterns of all the products in $(\text{Sm}_{0.5}\text{Gd}_{0.5})_2(\text{Ce}_{1-x}\text{Zr}_x)_2\text{O}_7$ were recorded in Fig. 1 and analyzed. Detailed analysis indicates that all XRD patterns match well with the standard cubic defect fluorite phase of CeO_2 . The diffraction peaks of $(\text{Sm}_{0.5}\text{Gd}_{0.5})_2(\text{Ce}_{0.7}\text{Zr}_{0.3})_2\text{O}_7$ located at 28.33°, 32.85°, 47.28°, and 56.21° can be well indexed to the (111), (200), (220), and (311) planes of a cubic fluorite

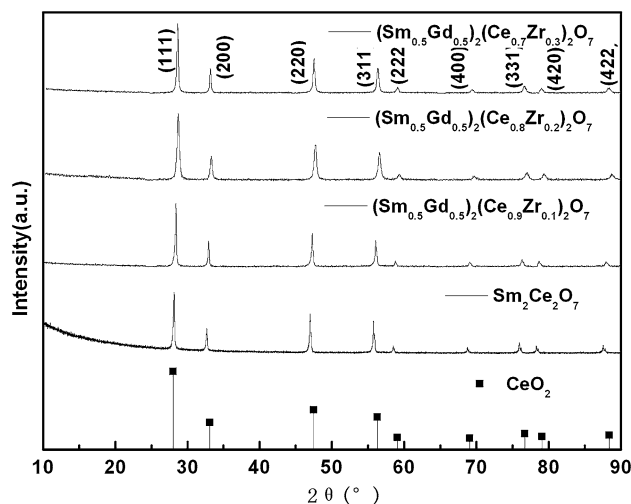


Fig. 1 XRD patterns of $(\text{Sm}_{0.5}\text{Gd}_{0.5})_2(\text{Ce}_{1-x}\text{Zr}_x)_2\text{O}_7$ ceramics

structure, respectively (Ref 27). In XRD patterns of other oxides, the defect fluorite structure can be identified by the scarce of super-lattice peaks at 2θ values between 32.85° and 47.28°. These two peaks could help us to distinguish the fluorite and pyrochlore structures (Ref 28). Furthermore, no peaks corresponding to the individual oxides are observed. This disparate feature can be attributed to the formation of $(\text{Sm}_{0.5}\text{Gd}_{0.5})_2(\text{Ce}_{1-x}\text{Zr}_x)_2\text{O}_7$ ceramics.

In the $\text{A}_2\text{B}_2\text{O}_7$ system, the crystal structure is mainly determined by the ionic radius ratio $r(\text{A}^{3+})/r(\text{B}^{3+})$ of A and B cations. The stable pyrochlore structure is limited to the range of $1.46 \leq r(\text{A}^{3+})/r(\text{B}^{3+}) \leq 1.78$, and the fluorite oxide will form if the $r(\text{A}^{3+})/r(\text{B}^{3+})$ is lower than 1.40 (Ref 29). For the complex rare-earth cerium oxides, the ionic radius can be estimated from the ionic radius of the component ions and the chemical composition using the following equation.

$$\frac{r(\text{A}_{\text{av}}^{3+})}{r(\text{B}_{\text{av}}^{4+})} = \frac{[0.5r(\text{Sm}^{3+}) + 0.5r(\text{Gd}^{3+})]}{[(1-x)r(\text{Ce}^{4+}) + xr(\text{Zr}^{4+})]}, \quad (\text{Eq 3})$$

where 0.5, 1-x, and x are the composition of each atom. The ionic radii of Sm^{3+} and Gd^{3+} are 1.079 and 1.053 Å, while the Zr^{4+} and Ce^{4+} are 0.72 and 0.97 Å, respectively. The values of $r(\text{A}_{\text{av}}^{3+})/r(\text{B}_{\text{av}}^{4+})$ for $(\text{Sm}_{0.5}\text{Gd}_{0.5})_2(\text{Ce}_{1-x}\text{Zr}_x)_2\text{O}_7$ oxides can be calculated by the Eq 3 with above mentioned ionic radiuses, and the values are equal to 1.11, 1.13, 1.156, and 1.189 with x increasing from zero to 0.3. The ionic ratios of $(\text{Sm}_{0.5}\text{Gd}_{0.5})_2(\text{Ce}_{1-x}\text{Zr}_x)_2\text{O}_7$ are smaller than 1.40 due to the co-doping in the Sm and Ce sites, which reveals that the co-doping in $\text{Sm}_2\text{Ce}_2\text{O}_7$ cannot change the crystal structure.

3.2 Microstructure

The typical microstructure of $(\text{Sm}_{0.5}\text{Gd}_{0.5})_2(\text{Ce}_{1-x}\text{Zr}_x)_2\text{O}_7$ ceramics is shown in Fig. 2. The average grain size of $(\text{Sm}_{0.5}\text{Gd}_{0.5})_2(\text{Ce}_{1-x}\text{Zr}_x)_2\text{O}_7$ ceramics is several micrometers. The interfaces between grains are very clean, the gap is very small, and no other inter-phases and unreacted oxides existed in boundaries between grains. The chemical compositions and relative density of the synthesized $(\text{Sm}_{0.5}\text{Gd}_{0.5})_2(\text{Ce}_{1-x}\text{Zr}_x)_2\text{O}_7$ ceramics are listed in Table 1. As can be seen from Table 1, the mole ratios of different elements in $(\text{Sm}_{0.5}\text{Gd}_{0.5})_2(\text{Ce}_{1-x}\text{Zr}_x)_2\text{O}_7$

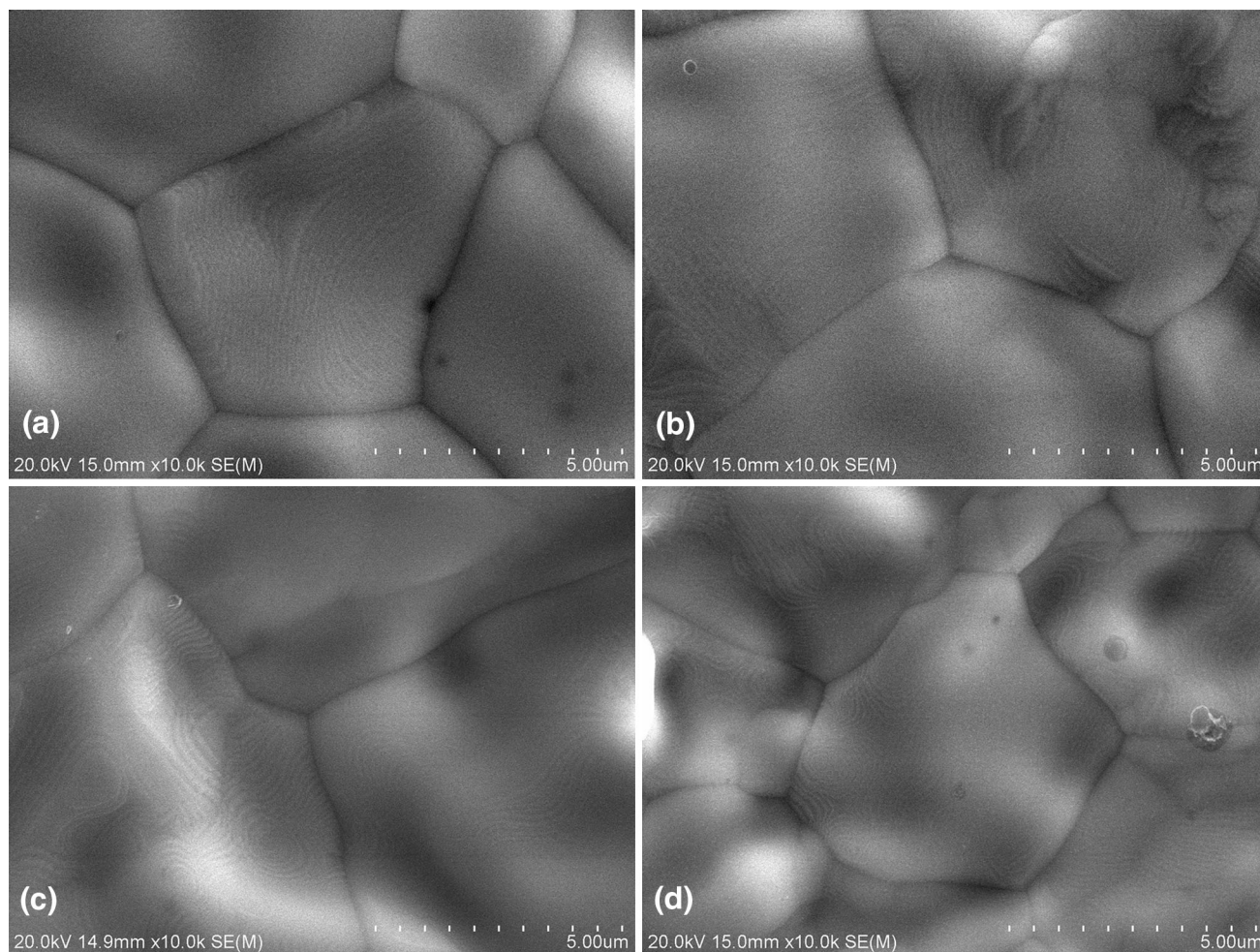


Fig. 2 Morphologies of $(\text{Sm}_{0.5}\text{Gd}_{0.5})_2(\text{Ce}_{1-x}\text{Zr}_x)_2\text{O}_7$ ceramics (a) $x = 0$, (b) $x = 0.1$, (c) $x = 0.2$, (d) $x = 0.3$

Table 1 Element mole ratio, relative density, and lattice parameter of $(\text{Sm}_{0.5}\text{Gd}_{0.5})_2(\text{Ce}_{1-x}\text{Zr}_x)_2\text{O}_7$ ceramics

Element composition	Mole ratio					Relative density	A (nm)
	Sm	Gd	Ce	Zr	O		
$x = 0$	6.9	8.7	18.9	0	65.5	97.5%	0.5475
$x = 0.1$	8.2	8.8	15.7	2.9	64.4	93.1%	0.5445
$x = 0.2$	8.5	8.6	14.9	3.5	64.5	94.8%	0.542
$x = 0.3$	8.4	8.2	14.1	4.7	64.6	97.1%	0.539

ceramics are very close to their stoichiometries, and each specimen has a high relative density due to the high-temperature sintering.

3.3 Thermal Expansion Coefficient

The dilatometric measurement results of $(\text{Sm}_{0.5}\text{Gd}_{0.5})_2(\text{Ce}_{1-x}\text{Zr}_x)_2\text{O}_7$ ceramics with calibration are plotted in Fig. 3. The typical linear expansions can be observed for $(\text{Sm}_{0.5}\text{Gd}_{0.5})_2(\text{Ce}_{1-x}\text{Zr}_x)_2\text{O}_7$ ceramics in the temperature range of 20–1000 °C. Clearly, there is no phase transformation for $(\text{Sm}_{0.5}\text{Gd}_{0.5})_2(\text{Ce}_{1-x}\text{Zr}_x)_2\text{O}_7$ ceramics in the temperature range. The technical thermal expansion coefficient is defined as

$$\alpha_{\text{tech}} = \frac{1}{L_0} \frac{\Delta L_k - \Delta L_0}{T_k - T_0}, \quad (\text{Eq 4})$$

where L_0 is the length of the specimen at T_0 (20 °C), ΔL_0 is the change in length at T_0 , and ΔL_k is the corresponding length change at temperature T_k .

Their calculated technical thermal expansion coefficients against temperature are plotted in Fig. 4, together with the data of YSZ. Fig. 4 shows that their thermal expansion coefficients increase smoothly with temperature up to 1000 °C, which is attributed to the increasing atomic spacing at elevated temperatures. As also can be seen in Fig. 4, the thermal expansion coefficient decreases gradually with increasing x from 0 to 0.3

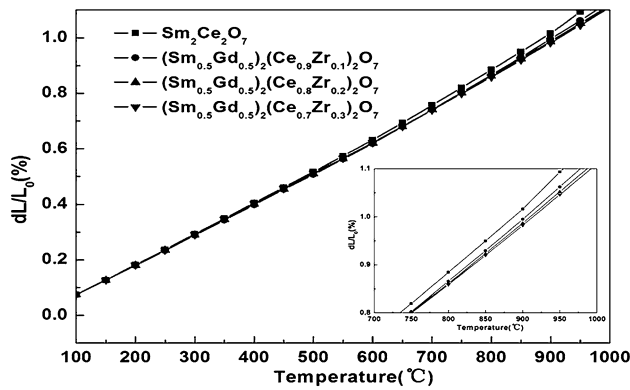


Fig. 3 Calibrated dilatometric data of $(\text{Sm}_{0.5}\text{Gd}_{0.5})_2(\text{Ce}_{1-x}\text{Zr}_x)_2\text{O}_7$ ceramics as function of temperature

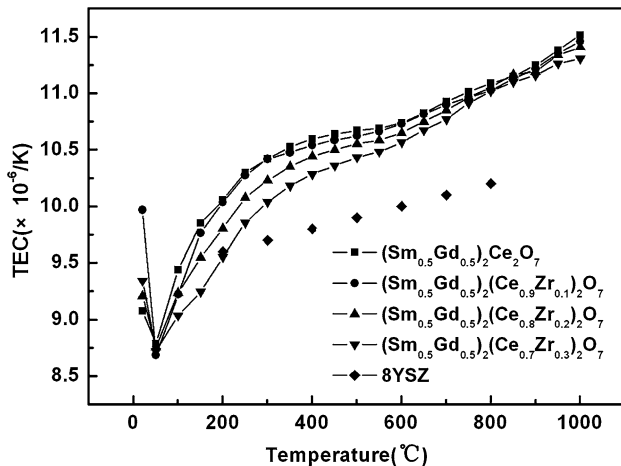


Fig. 4 Thermal expansion coefficients of $(\text{Sm}_{0.5}\text{Gd}_{0.5})_2(\text{Ce}_{1-x}\text{Zr}_x)_2\text{O}_7$ ceramics

at identical temperature levels. It is well known that the thermal expansion coefficient is inverse the crystal energy (U). The crystal (U) of an ionic compound can be expressed as (Ref 30).

$$U = \frac{N_0 A z^+ z^- e^2}{r_0} \left(1 - \frac{1}{n} \right), \quad (\text{Eq } 5)$$

where N_0 , A , z , r_0 , e , and n represent Avogadro's number, the Madelung constant, the ionic charge, the inter-ionic distance, the charge of an electron, and Born exponent, respectively. From the lattice parameters listed in Table 1, it can be known that the substitution of Zr^{4+} for Ce^{4+} results in a slight contraction in the unit cell, indicating a decrease in the average inter-ionic distance, r_0 . This would lead to an increase in the crystal energy of the $(\text{Sm}_{0.5}\text{Gd}_{0.5})_2(\text{Ce}_{1-x}\text{Zr}_x)_2\text{O}_7$ ceramics, which represents the decrease of thermal expansion coefficient. Alternatively, there are some structure defects, such as substitutional or interstitial cations and other imperfections in the lattice or varying properties in thermal expansion along with different orientations that have significant effect on the overall thermal expansion coefficient of $\text{A}_2\text{B}_2\text{O}_7$ oxides (Ref 31, 32). In the fluorite-type $\text{A}_2\text{Ce}_2\text{O}_7$ system, oxygen vacancies are randomly distributed in disordered fluorite structure; therefore, it facilitates formation of the ionic vacancy clustering, which represents to some extent the decrease in thermal

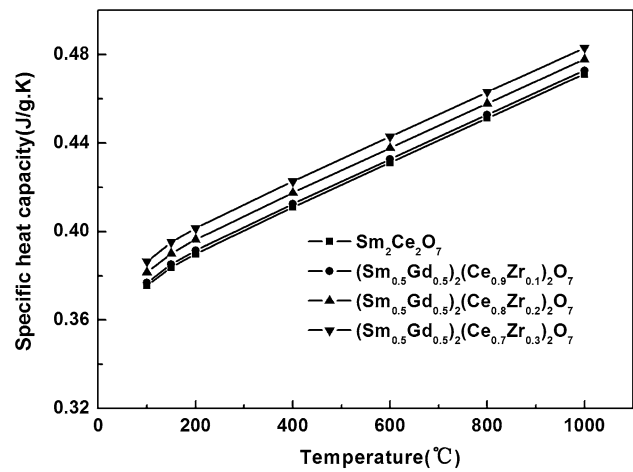


Fig. 5 The calculated specific heat capacities as a function of temperature for $(\text{Sm}_{0.5}\text{Gd}_{0.5})_2(\text{Ce}_{1-x}\text{Zr}_x)_2\text{O}_7$ ceramics

expansion. The structure disorder degree of fluorite-type $\text{A}_2\text{Ce}_2\text{O}_7$ is inverse to value of $r(A_{\text{av}}^{3+})/r(B_{\text{av}}^{4+})$ (Ref 29), and the increasing value of $r(A_{\text{av}}^{3+})/r(B_{\text{av}}^{4+})$ in $(\text{Sm}_{0.5}\text{Gd}_{0.5})_2(\text{Ce}_{1-x}\text{Zr}_x)_2\text{O}_7$ ceramics represents the increase of thermal expansion coefficient. Hence, the decrease of thermal expansion coefficients with increasing ZrO_2 content in $(\text{Sm}_{0.5}\text{Gd}_{0.5})_2(\text{Ce}_{1-x}\text{Zr}_x)_2\text{O}_7$ ceramics reveals that the influence of crystal energy is greater than oxygen vacancy (Ref 29, 33). These thermal expansion coefficients are obviously higher than 7 wt.% yttria-stabilized zirconia [$10.7 \times 10^{-6}/\text{K}$ at 1000 °C (Ref 10)] and are good enough to be used as thermal barrier coating materials in the industry condition.

3.4 Thermal Conductivity

The specific heat capacities of the $(\text{Sm}_{0.5}\text{Gd}_{0.5})_2(\text{Ce}_{1-x}\text{Zr}_x)_2\text{O}_7$ ceramics at different temperatures were calculated according to the Neumann-Kopp rule based on the reference specific heat values of Sm_2O_3 , Gd_2O_3 , CeO_2 and ZrO_2 . As can be seen in Fig. 5, the specific heat capacity of the $(\text{Sm}_{0.5}\text{Gd}_{0.5})_2(\text{Ce}_{1-x}\text{Zr}_x)_2\text{O}_7$ ceramics increases with increasing temperature from room temperature to 1000 °C, and the calculated specific heat capacity of the $(\text{Sm}_{0.5}\text{Gd}_{0.5})_2(\text{Ce}_{1-x}\text{Zr}_x)_2\text{O}_7$ ceramics slightly increases from $x = 0$ to 0.3 at identical temperature levels.

Fig 6 shows the composition-dependent thermal diffusivities of the $(\text{Sm}_{0.5}\text{Gd}_{0.5})_2(\text{Ce}_{1-x}\text{Zr}_x)_2\text{O}_7$ ceramics measured by laser flash method. The values of thermal diffusivity are the arithmetic mean of three measurements. Since the error derived from the mean standard deviation of the three measurements for each specimen is $<1.5\%$, the error bars in Fig. 6 are omitted for all thermal diffusivity data because they are smaller than symbols. As can be seen in Fig. 6, the thermal diffusivity of the $(\text{Sm}_{0.5}\text{Gd}_{0.5})_2(\text{Ce}_{1-x}\text{Zr}_x)_2\text{O}_7$ ceramics exhibits inverse temperature dependence, which suggests a dominant phonon conduction behavior in most polycrystalline materials (Ref 32, 33). Furthermore, the thermal diffusivity remarkably decreases with increasing Zr^{4+} fraction, and $(\text{Sm}_{0.5}\text{Gd}_{0.5})_2(\text{Ce}_{0.7}\text{Zr}_{0.3})_2\text{O}_7$ exhibits the lowest thermal diffusivity among all the ceramics investigated.

The thermal conductivities were calculated using Eq 1 and calibrated with Eq 2 to represent fully dense samples, as plotted in Fig. 7. The error bars are omitted because they are smaller

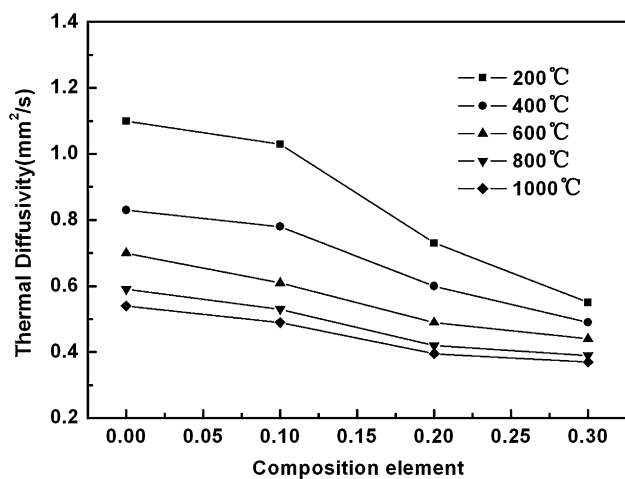


Fig. 6 Composition-dependent thermal diffusivities of $(\text{Sm}_{0.5}\text{Gd}_{0.5})_2(\text{Ce}_{1-x}\text{Zr}_x)_2\text{O}_7$ ceramics at different temperatures

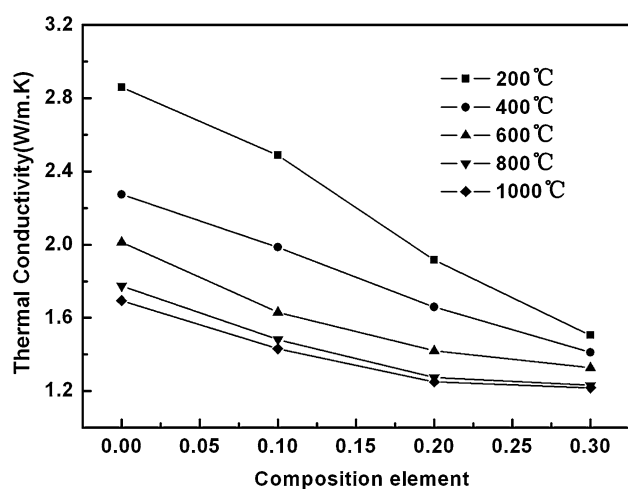


Fig. 7 Composition-dependent thermal conductivities of $(\text{Sm}_{0.5}\text{Gd}_{0.5})_2(\text{Ce}_{1-x}\text{Zr}_x)_2\text{O}_7$ ceramics

than the symbols. The thermal conductivity of the synthesized samples also decreases with increasing ZrO_2 content. It decreases from 1.69 W/m K for $\text{Sm}_2\text{Ce}_2\text{O}_7$ to 1.22 W/m K for $(\text{Sm}_{0.5}\text{Gd}_{0.5})_2(\text{Ce}_{0.7}\text{Zr}_{0.3})_2\text{O}_7$ at 1000 °C. The composition with $x = 0.3$ exhibits the lowest at all temperatures, and the thermal conductivities of $(\text{Sm}_{0.5}\text{Gd}_{0.5})_2(\text{Ce}_{1-x}\text{Zr}_x)_2\text{O}_7$ ceramics are obviously lower than those of fully dense 7 wt.%YSZ [3.0 at room temperature to 2.3 W/m K at 700 °C reported by Wu et al (Ref 31)]. In electronic insulator crystalline solids, heat is transferred by lattice vibrations. The quanta of lattice vibrations are defined as phonons, and the thermal conductivity is proportional to the phonon mean free path $l(\omega, t)$, which can be approximately described as reported in (Ref 33).

$$\frac{1}{l(\omega, t)} = \frac{1}{l_i(\omega, t)} + \frac{1}{l_p(\omega, t)} + \frac{1}{l_v(\omega, t)} + \frac{1}{l_{gb}}, \quad (\text{Eq 6})$$

where $l_i(\omega, t)$, $l_p(\omega, t)$, $l_v(\omega, t)$, and l_{gb} are the phonon mean free path due to interstitials scattering, point defect scattering, vacancies scattering, and grain boundary scattering, respectively. Since the phonon mean free path is several orders of

magnitude smaller than the grain size for the $(\text{Sm}_{0.5}\text{Gd}_{0.5})_2(\text{Ce}_{1-x}\text{Zr}_x)_2\text{O}_7$ ceramics, the grain boundary scattering can be omitted (Ref 34). The small phonon mean free path contributes to strong phonon scattering in the crystal cell. First, the special and complex crystal structure of fluorite-type $(\text{Sm}_{0.5}\text{Gd}_{0.5})_2(\text{Ce}_{1-x}\text{Zr}_x)_2\text{O}_7$ ceramics can reduce the phonon mean free path. The second factor is the intrinsic oxygen vacancies existed in the crystal lattice. The $(\text{Sm}_{0.5}\text{Gd}_{0.5})_2(\text{Ce}_{1-x}\text{Zr}_x)_2\text{O}_7$ ceramics could be regarded as the solid solution of Zr^{4+} taking the site of Ce^{4+} in $(\text{Sm}_{0.5}\text{Gd}_{0.5})_2\text{Ce}_2\text{O}_7$ ceramics. Thus, the last factor is the substitutional atoms existing in the lattice of $(\text{Sm}_{0.5}\text{Gd}_{0.5})_2\text{Ce}_2\text{O}_7$, which can also reduce the mean free path of phonon. Atomic substitution causes lattice distortion, increases phonon scattering, and decreases phonon mean free path, according to Eq 7 (Ref 35). On the other hand, the phonon mean free path is proportional to the square of atomic weight difference between the solute and host cations, according to Eq 8 (Ref 35):

$$\frac{1}{l(\omega, t)} = \frac{2ca^3\omega^4}{\pi v^4} J^2 \gamma^2 \left(\frac{\Delta R}{R} \right)^2 \quad (\text{Eq 7})$$

$$\frac{1}{l(\omega, t)} = \frac{a^3}{4\pi v^4} \omega^4 c \left(\frac{\Delta M}{M} \right)^2, \quad (\text{Eq 8})$$

where a^3 is the volume per atom, v the transverse wave speed, ω the phonon frequency, c the concentration per atom, J the constant, γ the Gruneisen parameter, M and R the average mass and ionic radius of the host atom, respectively, and ΔM and ΔR are the differences of masses and ionic radius between the substituted and substituting atoms, respectively. Because the atomic weights of Zr and Ce are 91.22 and 140.1, respectively. The effective ionic radii of Zr^{4+} and Ce^{4+} are 0.72 and 0.97 Å, and the effective phonon scattering of the substitutional atoms contributes to the lower thermal conductivity. Thus, thermal conductivity of $(\text{Sm}_{0.5}\text{Gd}_{0.5})_2(\text{Ce}_{1-x}\text{Zr}_x)_2\text{O}_7$ ceramics decreases with increasing ZrO_2 content at identical temperature levels. The low thermal conductivity indicates that the $(\text{Sm}_{0.5}\text{Gd}_{0.5})_2(\text{Ce}_{1-x}\text{Zr}_x)_2\text{O}_7$ ceramics can be explored as potential candidates for thermal barrier coating applications.

4. Conclusions

Pure $(\text{Sm}_{0.5}\text{Gd}_{0.5})_2(\text{Ce}_{1-x}\text{Zr}_x)_2\text{O}_7$ ceramics with fluorite structure were successfully prepared by solid-state reaction method and sintered at 1600 °C for 10 h using Sm_2O_3 , Gd_2O_3 , ZrO_2 and CeO_2 as raw materials. Their microstructure is very dense and there are no other inter-phases or unreacted oxides existing at the boundaries between grains. The thermal conductivity of $(\text{Sm}_{0.5}\text{Gd}_{0.5})_2(\text{Ce}_{1-x}\text{Zr}_x)_2\text{O}_7$ ceramics decreases with increasing ZrO_2 content at identical temperature levels, and phonon scattering caused by the substitutional atoms contributes to the low thermal conductivity. The thermal expansion coefficient of $(\text{Sm}_{0.5}\text{Gd}_{0.5})_2(\text{Ce}_{1-x}\text{Zr}_x)_2\text{O}_7$ ceramics decreases with increasing Zr^{4+} ions, and these thermal expansion coefficients are obviously higher than 7 wt.% yttria-stabilized zirconia. The synthesized $(\text{Sm}_{0.5}\text{Gd}_{0.5})_2(\text{Ce}_{1-x}\text{Zr}_x)_2\text{O}_7$ ceramics can be explored as potential candidates for thermal barrier coatings.

Acknowledgments

The authors gratefully acknowledge the financial support provided by Program for Science & Technology Innovation Talents in Universities of Henan Province (13HASTIT018) and Key Project in Science and Technology of Henan Province (132102210142).

Open Access

This article is distributed under the terms of the Creative Commons Attribution 4.0 International License (<http://creativecommons.org/licenses/by/4.0/>), which permits unrestricted use, distribution, and reproduction in any medium, provided you give appropriate credit to the original author(s) and the source, provide a link to the Creative Commons license, and indicate if changes were made.

References

1. R. Eriksson, S. Johansson, H. Brodin, E. Broitman, L. Ostergren, and X.H. Li, Influence of Substrate Material on the Life of Atmospheric Plasma Sprayed Thermal Barrier Coatings, *Surf. Coat. Technol.*, 2013, **232**, p 795–803
2. L.J. Gu, Z.Z. Fan, Y. Zhao, B.L. Zou, Y. Wang, S.M. Zhao, and X.Q. Cao, Influence of Ceramic Thickness on Residual Stress and Bonding Strength for Plasma Sprayed Doped Thermal Barrier Coatings on Aluminum Alloy, *Surf. Coat. Technol.*, 2012, **206**, p 440–4410
3. P.F. Zhao, C.A. Sun, X.Y. Zhu, F.L. Shang, and C.J. Li, Fracture Toughness Measurements of Plasma-Sprayed Thermal Barrier Coatings Using a Modified Four-Point Bending Method, *Surf. Coat. Technol.*, 2010, **204**, p 4066–4074
4. A. Afrasiabi, M. Saremi, and A. Kobayshi, A Comparative Study on Hot Corrosion Resistance of Three Types of Thermal Barrier Coatings: YSZ, YSZ + Al₂O₃ and YSZ/Al₂O₃, *Mater. Sci. Eng. A*, 2008, **478**, p 264–269
5. J.M. Drexler, K. Shinoda, A.L. Ortiz, D.S. Li, A.L. Vasiliev, A.D. Gledhill, S. Sampath, and N.P. Padture, Air Plasma Sprayed Thermal Barrier Coatings that are Resistant to High Temperature Attack by Glass Deposits, *Acta Mater.*, 2010, **58**, p 6835–6844
6. W. Chi, S. Sampath, and H. Wang, Ambient and High-Temperature Thermal Conductivity of Thermal Sprayed Coatings, *J. Thermal Spray Technol.*, 2006, **12**, p 772–777
7. H.B. Guo, S.K. Gong, K.A. Khor, and H.B. Xu, Effect of Thermal Expansion on the Microstructure and Properties of EB-PVD Gradient Thermal Barrier Coating, *Surf. Coat. Technol.*, 2003, **168**, p 23–29
8. G.D. Girolamo, C. Blasi, M. Schioppa, and L. Tapfer, Structure and Thermal Properties of Heat Treated Plasma Ceria-Yttria Co-stabilized Zirconia Coatings, *Ceram. Inter.*, 2010, **36**, p 961–968
9. S. Guo and Y. Kagawa, Effect of Thermal Exposure on Hardness and Young's Modulus of EB-PVD Yttria-Partially Stabilized Zirconia Thermal Barrier Coatings, *Ceram. Inter.*, 2006, **32**, p 263–270
10. L. Guo, H.B. Guo, G.H. Ma, M. Abbas, and S.K. Gong, Ruddlesden Popper Structured BaLa₂Ti₃O₁₀, a Highly Anisotropic Material for Thermal Barrier Coatings, *Ceram. Inter.*, 2012, **38**, p 4345–4352
11. M. Abbas, L. Guo, and H.B. Guo, Evaluation of Stress Distribution and Failure Mechanism in Lanthanum Titanium Aluminum Oxides Thermal Barrier Coatings, *Ceram. Inter.*, 2013, **39**, p 5103–5111
12. X.W. Song, M. Xie, and R.D. Mu, Influence of the Partial Substitution of Y₂O₃ with Ln₂O₃ (Ln = Nd, Sm, Gd) on the Phase Structure and Thermophysical Properties of ZrO₂-Nb₂O₅-Y₂O₃ Ceramics, *Acta Mater.*, 2011, **59**, p 3985–4902
13. F. Yang, X.F. Zhao, and P. Xiao, The Effects of Temperature and Compositions on the Thermal Conductivities of [(ZrO₂)_{1-x}(CeO₂)_x]_{0.92}(Y₂O₃)_{0.08} (0 < x < 1) Solid Solutions, *Acta Mater.*, 2012, **60**, p 914–922
14. J.Y. Xiang, S.H. Chen, J.H. Huang, H. Zhang, and X.K. Zhao, Phase Structure and Thermophysical Properties of Co-doped La₂Zr₂O₇ Ceramics for Thermal Barrier Coatings, *Ceram. Inter.*, 2012, **38**, p 3607–3612
15. Z.G. Liu, J.H. Ouyang, and Y. Zhou, Preparation and Thermophysical Properties of (Nd_xGd_{1-x})₂Zr₂O₇ Ceramics, *J. Mater. Sci.*, 2008, **43**, p 3596–3603
16. Z.C. Huang, J. Feng, and W. Pan, First-Principle Calculation of Structural and Thermodynamic Properties of Y₃Al₅O₁₂, *Solid State Comm.*, 2011, **151**, p 1559–1563
17. X.Y. Xie, H.B. Guo, S.K. Gong, and H.B. Xu, Lanthanum-Titanium-Aluminum Oxide: A Novel Thermal Barrier Coating Material for Application at 1300 °C, *J. Eur. Ceram. Soc.*, 2011, **31**, p 1677–1683
18. Z.H. Song, L.J. Guo, L. Gang, Z. Zheng, and W.X. Li, Investigation About Thermophysical Properties of Ln₂Ce₂O₇ (Ln = Sm, Er and Yb) Oxides for Thermal Barrier Coatings, *Mater. Res. Bull.*, 2012, **47**, p 4181–4186
19. J. Feng, B. Xiao, R. Zhou, W. Pan, and D.R. Clarke, Anisotropic Elastic and Thermal Properties of the Double Perovskite Slab-Rock Slat Layer Ln₂SrAl₂O₇ (Ln = La, Nd, Sm, Eu, Gd or Dy) Natural Super-Lattice Structure, *Acta Mater.*, 2012, **60**, p 3380–3392
20. G. Lei, G.H. Bo, P. Hui, and G.S. Kai, Thermophysical Properties of Yb₂O₃ Doped Gd₂Zr₂O₇ and Thermal Cycling Durability of (Gd_{0.9}Yb_{0.1})₂Zr₂O₇/YSZ Thermal Barrier Coatings, *J. Eur. Ceram. Soc.*, 2014, **34**, p 1255–1263
21. L.H. Ran, W.C. An, and Z.C. Guang, Low Thermal Conductivity Sr²⁺, Zn²⁺ and Ti⁴⁺ ions Doped LaMgAl₁₁O₁₉ for Potential Thermal Barrier Coating Applications, *Ceram. Inter.*, 2014, **40**, p 16273–16279
22. C.X. Ge, Y.S. Qing, Z.H. Song, L. Gang, L.Z. Jun, R. Bo, D.X. Dan, Z.H. Ming, and T. An, Preparation and Thermophysical Properties of (Sm_{1-x}Er_x)₂Ce₂O₇ Oxides for Thermal Barrier Coatings, *Mater. Res. Bull.*, 2014, **51**, p 171–175
23. H. Yamamura, H. Nishino, K. Kakinuma, and K. Nomura, Electrical Conductivity Anomaly Around Fluorite-Pyrochlore Phase Boundary, *Solid State Ion.*, 2003, **158**, p 359–365
24. C.L. Wan, Z.X. Qu, A.B. Du, and W. Pan, Influence of B Site Substituent Ti on the Structure and Thermophysical Properties of A₂B₂O₇-type Pyrochlore Gd₂Zr₂O₇, *Acta Mater.*, 2009, **57**, p 4782–4789
25. L. Ling, X. Qiang, W.F. Chi, and Z.H. Song, Thermophysical Properties of Complex Rare-Earth Zirconate Ceramic for Thermal Barrier Coatings, *J. Am. Ceram. Soc.*, 2008, **91**, p 2398–2401
26. D.J. Leitner, P. Chuchvalec, and D. Sedmidubsky, Estimation of Heat Capacity of Solid Mixed Oxides, *Thermochim. Acta*, 2003, **395**, p 27–46
27. W.C. Jie, H.W. Zhi, and W. Yue, Synthesis of Monodispersed La₂Ce₂O₇ Nanocrystals via Hydrothermal Method: A Study of Crystal Growth and Sintering Behavior, *Int. J. Refractory Metals. Hard Mater.*, 2012, **31**, p 242–246
28. Z.J. Hua, Y.J. Shun, and C. Xun, Thermal Expansion and Solubility Limits of Cerium-Doped Lanthanum Zirconates, *J. Alloys. Compds.*, 2012, **525**, p 78–82
29. M.A. Subramanian, G. Aravamudan, and G.V.S. Rao, Oxides Pyrochlore—A Review, *Prog. Solid State Chem.*, 1983, **15**, p 55–143
30. W.D. Kingery, H.K. Bowen, and D.R. Uhlmann, *Introduction to Ceramics*, 2nd ed., Wiley, New York, 1976
31. J. Wu, X.Z. Wei, P.G. Padture, and M. Gell, Low-thermal-Conductivity-Rare-Earth Zirconates for Potential Thermal-Barrier-Coating Applications, *J. Am. Ceram. Soc.*, 2002, **85**, p 3031–3035
32. H. Lehmann, D. Pitzer, G. Pracht, R. Vassen, and D. Stover, Thermal Conductivity and Thermal Expansion Coefficients of the Lanthanum Rare-Earth-Element Zirconates System, *J. Am. Ceram. Soc.*, 2003, **86**, p 1338–1344
33. K. Shimamura, T. Arima, K. Idemitsu, and K. Inagaki, Thermophysical Properties of Rare-Earth Stabilized Zirconia and Zirconia Pyrochlores as Surrogates for Actinide-Doped Zirconia, *Int. J. Thermophys.*, 2007, **28**, p 1074–1084
34. P.G. Klemens, The Scattering of Low-Frequency Lattice Waves by Static Imperfections, *Proc. Phys. Soc.*, 1955, **73**, p 1113–1128
35. Z.H. Song, L.J. Guo, C.X. Ge, and W.X. Li, Preparation, Characterization, and Thermophysical Properties of (La_{0.95}Sr_{0.05})₂Ce₂O_{6.95} Ceramics for Thermal Barrier Coatings, *Int. J. App. Ceram. Technol.*, 2013, **1–9**, p 1–12